59th ILLMENAU SCIENTIFIC COLLOQUIUM
Technische Universität Illmenau, 11 - 15 September 2017
URN: urn:nbn:de:gbv:ilm1-2017iwk-065:1

ENHANCED MEASUREMENT ROUTINE FOR OPTICAL 3D GEOMETRY MEASUREMENT OF HOT SPECIMEN BY REDUCTION OF AMBIENT PRESSURE

Lorenz Quentin[1], Rüdiger Beermann[1], Andreas Pösch[1], Eduard Reithmeier[1], and Markus Kästner[1]*

[1]Institute of Measurement and Automatic Control, Leibniz Universität Hannover

[*]Corresponding author. Email: Lorenz.Quentin@imr.uni-hannover.de

ABSTRACT

Optical 3d geometry measurement is a vital part of the process control when manufacturing hybrid components. These so-called Tailored Forming components are meant to be inspected fast, in hot state and with high accuracy. In this paper, we examine the effect of a pressure reduction on the optical measurement data of hot objects, obtained with a self-developed fringe projection system. For this purpose, the fringe projection system has been attached to the window of vacuum chamber, housing a heatable cylinder as measurement object. Additionally, basic information on light propagation in inhomogeneous refractive index fields is provided next to a short review of previous work – including a theoretical analysis of a pressure reduction on the refractive index of air.

Index Terms - 3d measurement, optics, structured light, fringe projection, inline inspection, hot measurement object, refractive index of air

1 INTRODUCTION

Process automation and objective quality control are of vital importance in the production of high quality products. Within the Collaborative Research Centre (CRC) 1153 a process chain for hybrid components is developed. These so-called Tailored Forming components are required to be inspected as fast as possible in between each process step. In addition – to minimise the energy consumption for re-heating between subsequent hot forming procedures – it is not desirable to wait for the components to cool down, but rather to characterize the components' quality in hot state.
Optical 3d geometry measurement techniques based on the triangulation principle – such as the fringe projection method – satisfy the strict measurement requirements well, as a measurement task can be performed without contact of the hot components and in a short period of time.
As the heat transfer of hot objects into the surrounding air induces a density loss, the refractive index of air is reduced as well, resulting in a manipulation of the path of light. Therefore, the accuracy of optical geometry measurements is affected when measuring hot objects, as triangulation methods rely on the rectilinear propagation of light.
To fully understand the objective of this paper, initially some basic information on light

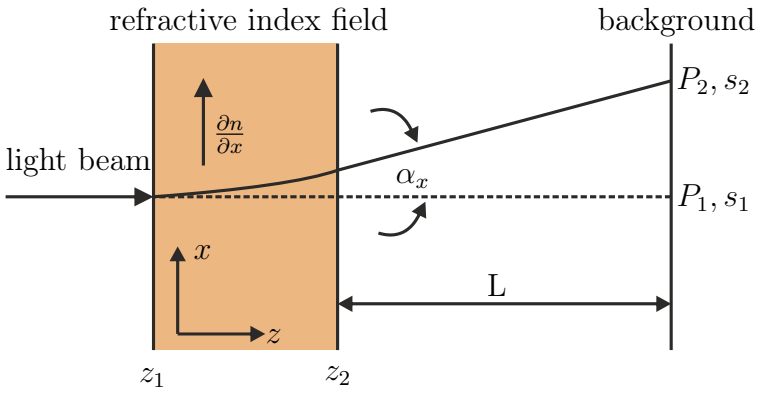

Figure 1: Schematic outline of manipulated light path due to an inhomogeneous refractive index field in a transparent medium according to Eckelmann [1]. The dashed line indicates the undisturbed light path, resulting in light location P_1 and optical path s_1 on the background. The solid line represents the light path induced by the refractive index field of width $\Delta z = z_2 - z_1$ with gradient $\frac{\partial n}{\partial x}$, resulting in location P_2 and an optical path difference $\Delta s = s_2 - s_1$. In the displayed example $\frac{\partial n}{\partial x}$ is greater zero – therefore the light beam is deflected towards the more dense air layers, in this scenario upwards. L is the distance between the right edge of the refractive index field and the background, α_x is the angle between deflected and undisturbed light path.

propagation in inhomogeneous refractive media is provided, as well as information on previous work, including results of 2d refractive index field measurements above a cylindrical object and a theoretical review of the refractive index of air depending on pressure and temperature according to Ciddor.
Using an experimental set-up – comprising a self-developed fringe projection system with two cameras, bandpass filters and a vacuum chamber with measurement window and heatable ceramic cylinder – the effect of the inhomogeneous refractive index field in air around a hot, cylindrical measurement object as a function of pressure is examined by conducting geometry measurements in different pressure configurations.

2 THEORETICAL AND EXPERIMENTAL BACKGROUND

2.1 Physical Basics

Triangulation-based measurement systems rely on rectilinear light propagation. As hot objects inevitably manipulate the surrounding air's density field, the light emitted from the illumination unit will not propagate in a straight line. The amount of light deflection induced by the density-coupled refractive index field therefore affects the accuracy of the triangulation sensor. A schematic outline of a light beam traversing such a transparent, inhomogeneous refractive index field is displayed in figure 1.

$$\overline{P_2P_1} = L \int_{z_1}^{z_2} \frac{1}{n_0} \frac{\partial n}{\partial x} \, \mathrm{d}z, \tag{1}$$

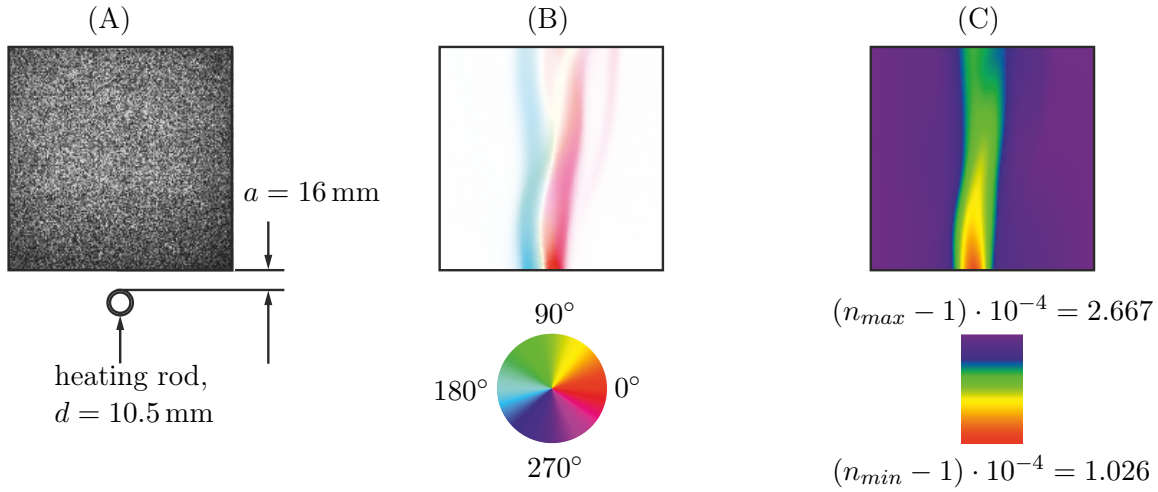

Figure 2: Background oriented schlieren measurement approximately 16 mm above a heated, cylindrical ceramic rod with a temperature of about 1020 °C according to Beermann et al. [4]. (A) Wavelet background with circular cross section of the ceramic heating rod. (B) Detected displacement field: The pixel displacement is encoded using the hsv colour space. The colour indicates the orientation of the displacement, the saturation represents the norm of the displacement vector. (C) 2d refractive index field derived by integration of corresponding displacement field.

$$\Delta s = s_2 - s_1 = \int_{z_1}^{z_2} (n - n_0)\, \mathrm{d}x. \tag{2}$$

The light beam is deflected, resulting in a light shift $\overline{P_2P_1}$ and an optical path difference Δs. Mathematical relationships for $\overline{P_2P_1}$ in x-direction and Δs obeying Fermat's principle are given in equations 1 and 2 (according to Eckelmann [1]), with L being the distance between the right edge of the refractive index field and the background, Δz being the width of the field, n_0 being the initial refractive index value of air and α_x being the angle between the manipulated and undisturbed light path.

2.2 Convective Heat Flow Above Hot Cylindrical Objects

Meier et al. [2, 3] exploited the induced light shift $\overline{P_2P_1}$ (figure 1) to measure 2d density fields in transparent media by deriving the *background oriented schlieren method*. Beermann et al. [4] applied the background oriented schlieren method to visualize and quantify the inhomogeneous refractive index field in air above a hot, cylindrical measurement object and compared the obtained results to heat flow simulations implemented with the software *Comsol Multiphysics* [5]. An exemplary measurement result of the 2d refractive index field in air – approximately 16 mm above a ceramic heating rod, with a temperature of about 1020 °C and a diameter $d = 10.5\,\mathrm{mm}$ – is given in figure 2.

If the whole 3d geometry data of a hot measurement object is meant to be characterised simultaneously in *one shot* with radially arranged fringe projection sensors, the greatest

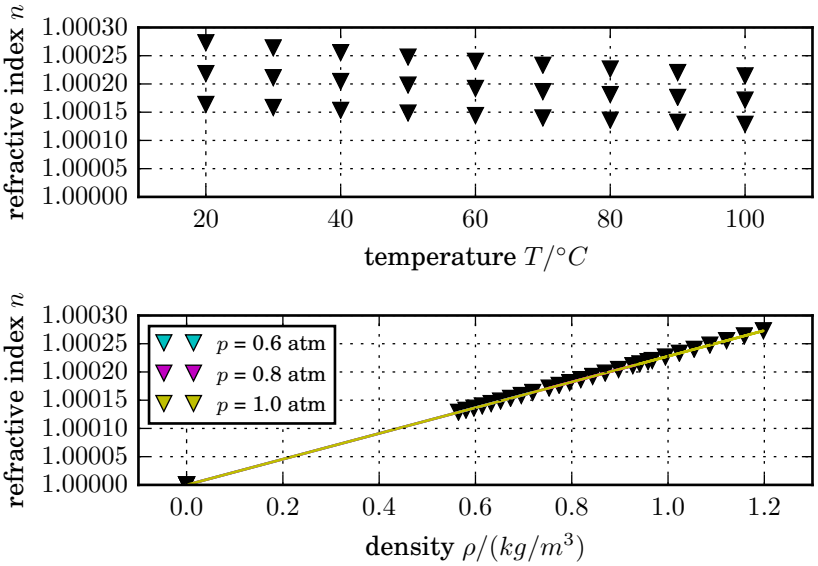

Figure 3: Refractive index of air as a function of temperature and density for different ambient pressure values according to Beermann et al. [6]. The temperature-refractive-index-relationship has been gained by evaluating Ciddor's equation for a wavelength of $\lambda = 532\,\mathrm{nm}$, a constant CO_2-concentration of $450\,\frac{\mu mol}{mol}$ and a relative humidity that has been set to a value of 55 % for a temperature of 20 °C and an ambient pressure of 1 atm. The change in relative humidity due to temperature increase and pressure reduction has been respected in the given range of validity of Ciddor's equation.

light path manipulations will most probably occur directly above the hot object – due to the high gradients in the refractive index field based on the convective heat flow.

2.3 Simulation: Effect of Pressure Reduction on Refractive Index Field

As the amount of light deflection is directly coupled not only to the expansion and shape, but also to the gradient of the refractive index field (compare to equation 1), a reduction of the gradient leads to a decrease in light deflection. Beermann et al. [6] investigated the effect of a pressure reduction in air on the light path shift of a virtual laser illumination unit by conducting 2d heat transfer and ray tracing simulations.
In a first simulation step, the density fields in air around a hot steel cylinder – incorporating temperatures up to 1200 °C – have been simulated under different pressure conditions. In a second step, the 2d density information has been used to derive the corresponding 2d inhomogeneous refractive index fields in order to execute ray tracing simulations. The density-refractive-index-coupling has been gained via extrapolated *Ciddor's equation* [7]. The expected validity range of Ciddor's equation for dry air has been given by *The National Institute of Standards and Technology* (NIST) [8] for pressure values between 60 kPa and 120 kPa and air temperature values between −40 °C and 100 °C. The Tailored Forming components can incorporate temperatures above 1000 °C, resulting in air temperatures highly above the given range of validity. Therefore Ciddor's equation has been linearly ex-

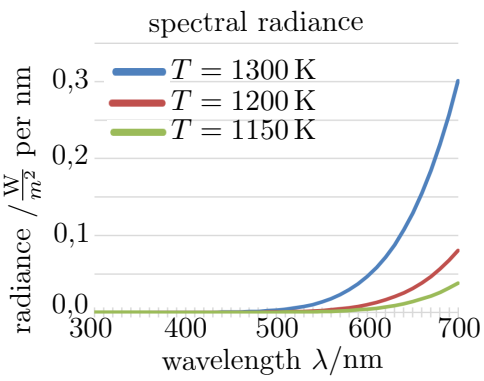

(A)

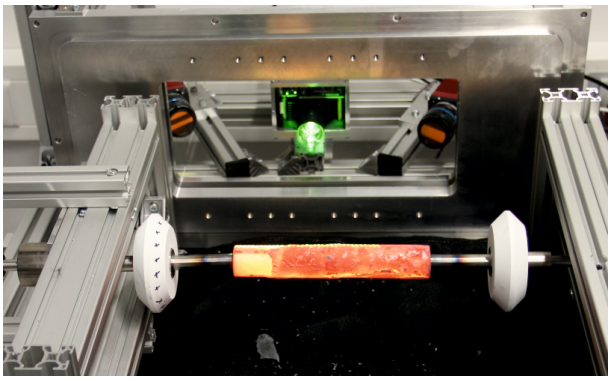

(B)

Figure 4: (A) Black body radiation according to *Planck's law* for three exemplary body temperatures. The emitted energy at a wavelength of 600 nm and a temperature of 1200 K is about 22-times higher than for a wavelength of 500 nm. Therefore green ligth is used for the projected fringe patterns.(B) Red-glowing cylindrical component ($T \approx 1300\,\mathrm{K}$) securely fixed in front of a fringe projection system.

trapolated, making the assumption, that in ideal vacuum the refractive index of air is one (compare to figure 3, lower graph). A pressure reduction from 1 atm to 0.6 atm in a temperature range from 20 °C up to 100 °C leads to a reduction of the corresponding Δn-value: It follows for $\Delta n_{1\,\mathrm{atm}} = n_{100\,^\circ\mathrm{C}} - n_{20\,^\circ\mathrm{C}} = 5.8625 \cdot 10^{-5}$, whereas the same temperature range for 0.6 atm yields a smaller Δn-value with $\Delta n_{0.6\,\mathrm{atm}} = n_{100\,^\circ\mathrm{C}} - n_{20\,^\circ\mathrm{C}} = 3.5147 \cdot 10^{-5}$. A pressure reduction of 40 % therefore also results in a reduction of Δn by 40 %. The corresponding light deflections in such a refractive index field are decreased in similar scale.

2.4 Contrast Problems Due To Self-Radiation

Another challenge that arises is due to electromagnetic self-radiation of hot objects: The cylindrical measurement object in figure 4 (B) is glowing red – the measurement light of the triangulation sensor is superimposed by unwanted object-emitted light signals. In figure 4 (A) the black body radiation for three exemplary object temperatures is given according to Planck's law. The emitted energy for an object temperature of 1200 K at a wavelength of 600 nm is approximately 22-times higher than at a wavelength of 500 nm. Stöbener et al. [9] therefore recommend the usage of green measurement light and a green bandpass filter in front of the camera of an optical distance sensor, to extract the measurement signal (green) from all incoming radiation. First tests with the self-developed fringe projection system using a DLP-projector with green LEDs ($\lambda = 532\,\mathrm{nm}$) and a green bandpass filter with a bandwidth of 80 nm yielded enough contrast to realize the desired measurements.

3 EXPERIMENTAL SETUP

The set-up of the fringe projection unit (see fig. 5) contains two CMOS cameras (4,5) with machine vision lenses and green bandpass filters and one high-power green-LED DLP-projector (3). The fringe projection unit is mounted on aluminium profiles. The profiles are connected to a triangular framework to provide good stiffness of the cameras-projector-unit and are additionally fixated on the window cover plate (2) of a vacuum chamber. Inside the vacuum chamber, the measurement object (1) is also profile-mounted and fixated to the bottom of the chamber. The whole set-up can be rotated around the axial direction ξ of the cylindrical measurement object without changing the triangulation angle of the fringe projection unit.

4 RESULTS

All results are obtained by measuring the object through different shapes and developments of the refractive index field. The 3d points are then imported into GOM Inspect 2017 [10] and their geometry is evaluated using GOM's cylinder fit, which excludes points based on the $\pm 3\sigma$-band.
In this section, the results from earlier publications are re-evaluated using an enhanced evaluation method (see section 4.1). The used measurement object is shown on the bottom of figure 5 (C). Also, new results are obtained by measuring directly the geometry of the ceramic heating element (see top of figure 5 (D)), which incorporates temperatures of approximately 1020 °C and is therefore glowing red.

4.1 Enhanced Evaluation Method

Homogeneous heating of the measurement objects could not be assured during earlier experiments. The hollow steel cylinder heated from inside has a significant temperature gradient in axial direction of the cylinder (see fig. 6). In prior evaluations GOM's cylinder fit was feeded on all measured points, disregarding cylindricity and different expansion due to inhomogeneous heating.
The measured 3d points are now evaluated sub-area-wise, namely in stripes of 2-3 mm in length (still including about 5000 3d points each) instead of analysing the whole cylinder data altogether. The length difference ($<5\%$ of original length) reduces the absolute temperature gradient within the evaluated sub-area to a negligible amount. Figure 7 shows four example regions on the 3d points of the measured heating element.
The main advantage of this method is its independence to the overall object deformation by inhomogeneous heating. Nevertheless, the qualitative interpretation of the results is not impaired by sub-area-wise fitting procedure.

4.2 Re-Evaluation of Prior Results

In this section, the results from Quentin et al. [11, 12] are re-evaluated using the enhanced method according to section 4.2 to show the dependency of the calculated radius from

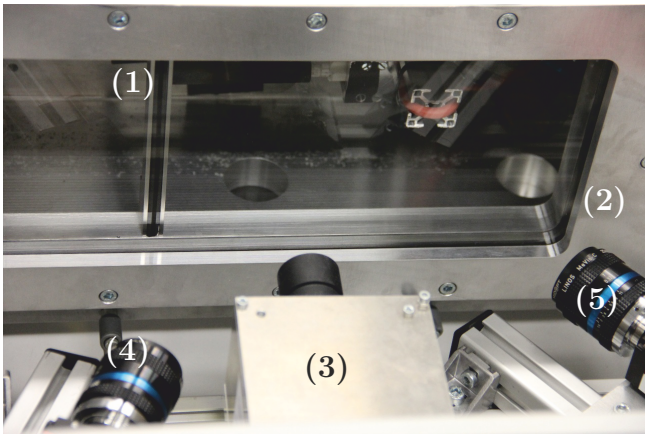

(A)

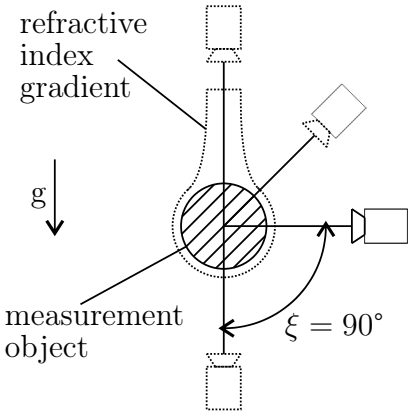

(B)

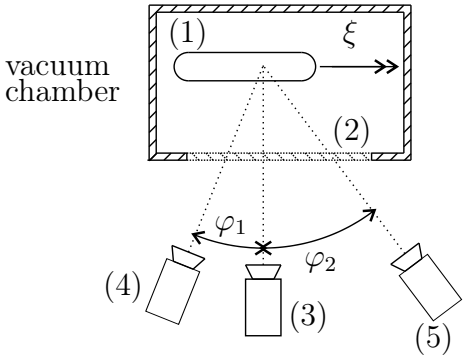

(D)

(E)

Figure 5: (A,C) Image and schematic of the experimental set-up with fringe projection system in front of the vacuum chamber: 1) Measurement object on heating element inside vacuum chamber, 2) protective window in cover plate of the vacuum chamber, 3) DLP-projector, 4) and 5) CMOS-cameras with machine vision lens and bandpass filters. Only displayed in (C): Body of vacuum chamber. In the following, fps (a) consists of the projector (3) and the left camera (4), it's triangulation angle is $\varphi_1 = 24°$. fps (b) contains (3) and (5), it's triangulation angle is $\varphi_2 = 38°$. (B) Different poses of fringe projection system measuring through different shapes of refractive index field. The pose is denoted by the angle ξ, with $\xi = 0°$ when measuring from below and $\xi = 180°$ when measuring from above. (D) Two different measurement objects. Top: Heating rod, length 81 mm, radius 5.25 mm, temperature when measured 1020 °C. Bottom: Stainless, hollow steel cylinder, length 60 mm, radius 8.5 mm, temperature when measured 480 °C.

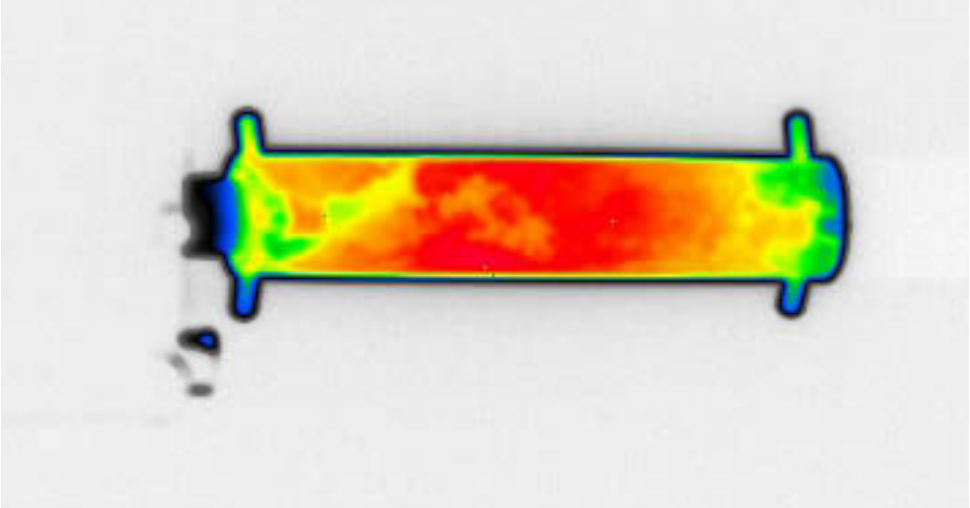

Figure 6: Qualitative thermal image of stainless steel cylinder. The thermal image shows an inhomogeneous temperature development.

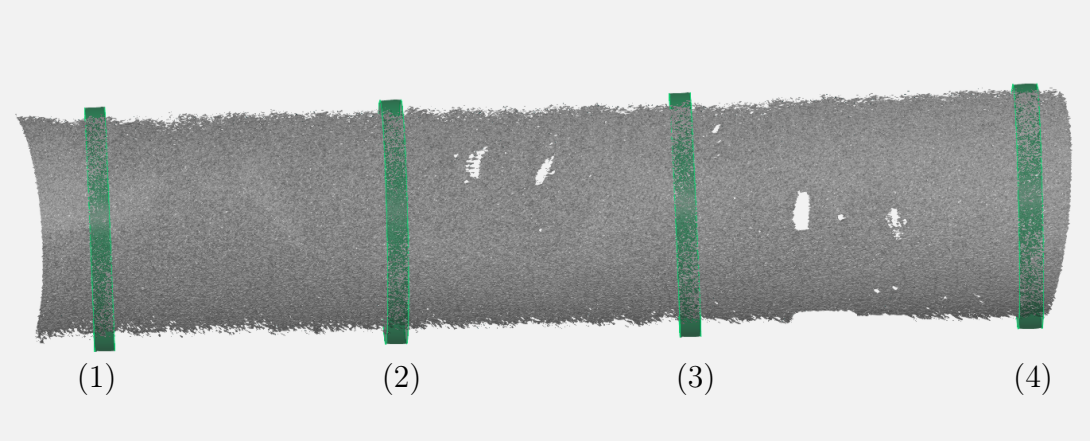

Figure 7: Small stripes of evaluated data on the measured 3d points of the stainless steel cylinder. The numbers in the image are corresponding to those in the measurement diagrams.

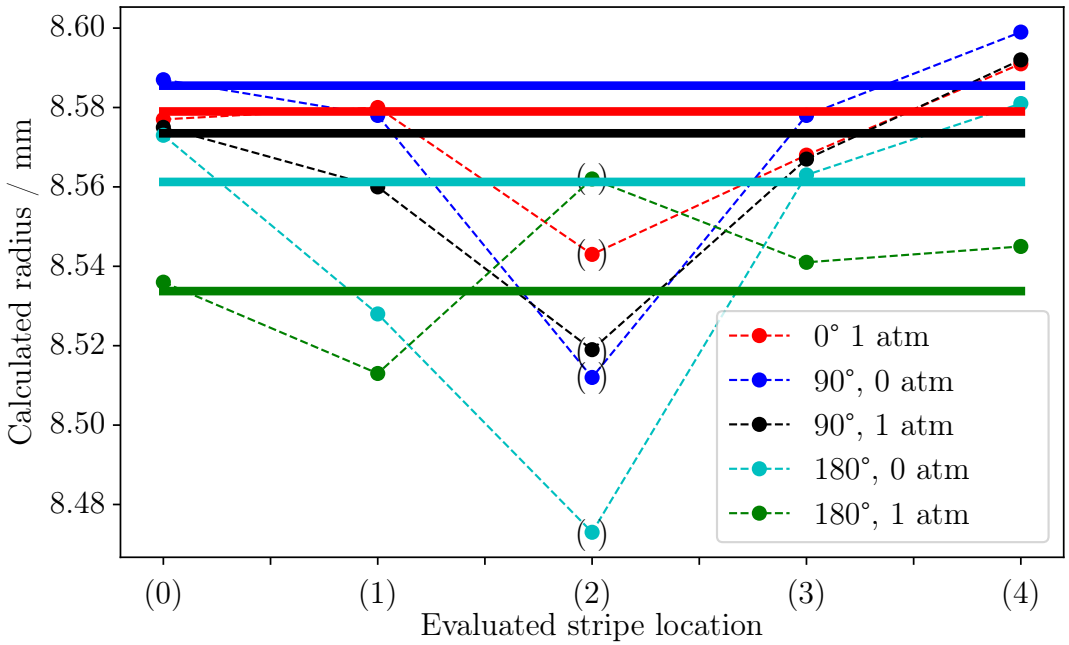

Figure 8: Measurement results for stainless steel cylinder (compare to figure 5 (D) at the bottom) at about 480 °C using fps (a) according to [11, 12]. The fitted radii are given at different surface locations according to the legend in figure 7, different poses according to figure 5 (B) and for a pressure of 1 and 0 atm respectively. Evaluated stripe location (0) represents the whole cylinder data set, whereas the stripe data in locations (1) - (4) are evaluated individually. Dashed lines: Averaged radius according to fitting procedure based on three individual cylinder data sets. Solid lines: Averaged radius based an all measurement locations for a certain measurement scenario. Stripe location (2) is not taken into account for the average, since it's data contradicts the clearly visible trendin the majority of data points.

optical 3d geometry measurements through different shapes and development phases of a heat-induced refractive index field.
A summary of the results is shown in figure 8. The average fitted radii is shrinking through the measurements. The radius of measurements at ($\xi = 90°, p = 0\,\text{atm}$) is about 7 µm larger than at ($\xi = 0°, p = 1\,\text{atm}$). From there, the third largest radius was calculated on the measurements at ($\xi = 90°, p = 1\,\text{atm}$), 5 µm smaller than the prior. The measurements at ($\xi = 180°, p = 0\,\text{atm}$) and ($\xi = 180°, p = 1\,\text{atm}$) traverse the most affected distance times refractive index difference $\Delta n \cdot d(\Delta n)$ and have the lowest calculated radii at an average of 8.561 mm and 8.534 mm respectively.
The results are, except for stripe number (2), very consistent within themselves. As expected and already referred to in [11], the fitted radius is shrinking when the light traverses an area with higher refractive index gradient and greater field expansion. When comparing both calculated radii at ($\xi = 90°, p = 0\,\text{atm}$) and ($\xi = 180°, p = 0\,\text{atm}$), it becomes very clear that applying vacuum does not fully eliminate the effect of the refractive index gradient on the optical 3d reconstruction by fringe projection.

4.3 Evaluation of New Results

In this section, the analysed measurement data was gained by measuring the ceramic heating rod displayed in figure 5 (D) at the top. The ceramic rod has been heated up to temperatures of about 1020 °C. Since the refractive index of air around a hot object is connected to the object's temperature, a bigger light deflection effect is expected, compared to the hollow steel cylinder at 480 °C. The measurements have been executed from the side ($\xi = 90°$), since this is the most likely measurement position in the process-chain-to-implement. Measuring the hot object from below might be affected by flying oxide scale, whereas the light deflection effect induced by the refractive index field is to large when measuring from the top.
The results of the measurements are displayed in figure 9. A minimum of ten measurements were used for each point on display. There is a clear trend in both subfigure 9 (A) and (B): The calculated fitting radius of the heating rod is rising when lowering the ambient pressure. The difference for fps (a) is about 6.8 µm from $p = 0.5\,\text{atm}$ to $p = 0\,\text{atm}$. The measurement at $p = 1.0\,\text{atm}$ has an averaged fitted radius of 5.316 mm, i.e. about 10 µm smaller than at $p = 0\,\text{atm}$.
For fps (b) the difference of the averaged fitted radius is about 4.4 µm from $p = 0.5\,\text{atm}$ to $p = 0.0\,\text{atm}$. Again, the measurement at $p = 1.0\,\text{atm}$ has the smallest fitted radius of 5.327 mm, which is about 9.4 µm smaller than at $p = 0.0\,\text{atm}$.

5 DISCUSSION OF RESULTS

In this section the effect of the inhomogeneous refractive index field in different developments on optical 3d geometry acquisition by fringe projection is discussed. First, the influence of a simplified refractive index field, consisting of two areas of different refractive indices, separated by a sharp boundary, on multiple view geometry is discussed. Later,

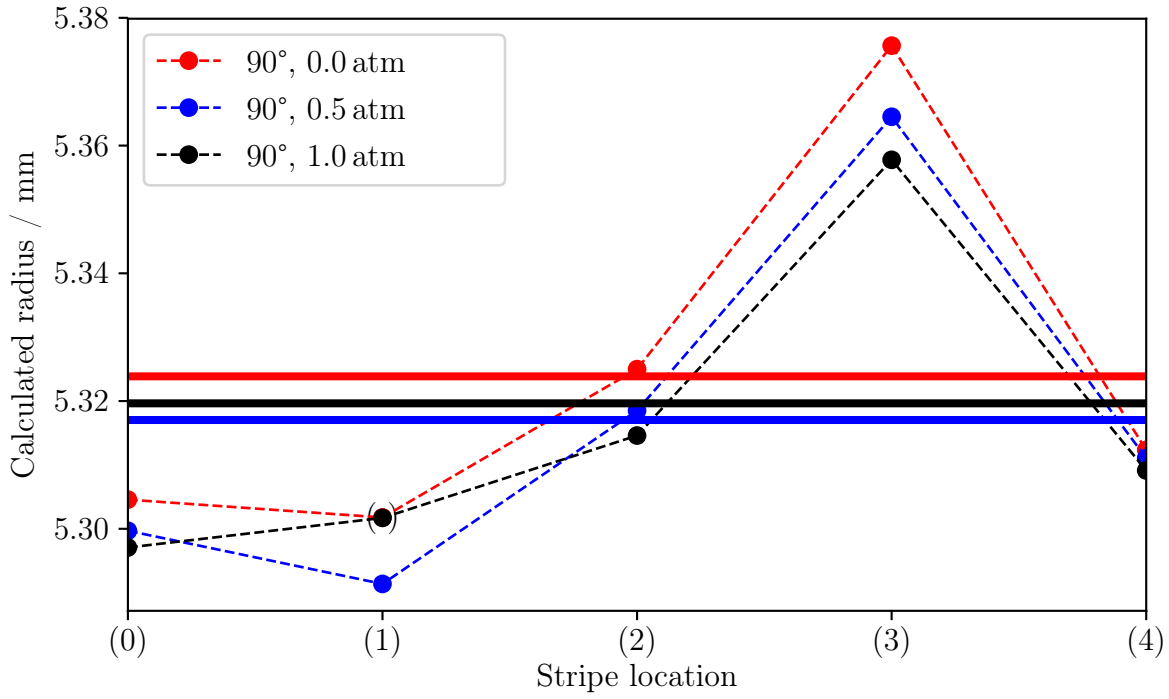

(A)

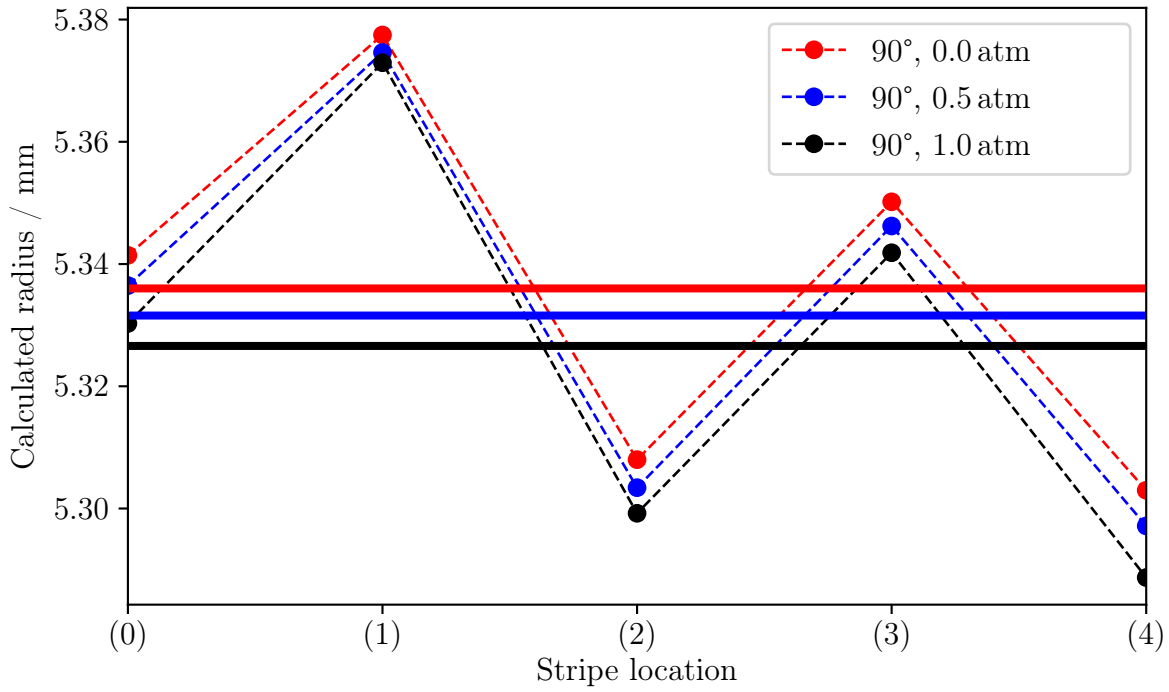

(B)

Figure 9: Measurement results for heating element (compare to figure 5 (D) at the top) at about 1020 °C using (A): fps (a) and (B): fps (b). The fitted radii are given at different surface locations according to the legend in figure 7 and for a pressure of 1, 0.5 and 0 atm respectively. Evaluated stripe location (0) represents the whole cylinder data set, whereas the stripe data in locations (1) - (4) are evaluated individually. Dashed lines: Averaged radius according to fitting procedure based on three individual cylinder data sets. Solid lines: Averaged radius based an all measurement locations for a certain measurement scenario. For fps (a) at 1 atm, stripe location (1) is not taken into account for the average since it's data clearly contradics the evident trend.

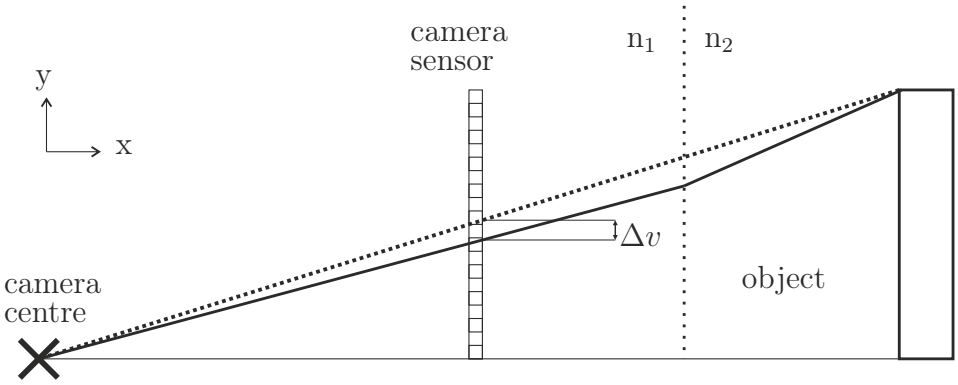

Figure 10: Lines of sight unaffected $n_1 = n_2$ (dotted) and affected $n_1 > n_2$ (solid) by a refractive index field. The object appears to be smaller when viewed through the refractive index n_2. The refractive indices are exagarrated for displaying purposes and are $n_1 = 1.5$, $n_2 = 1.0$.

other effects on the measurements are pointed out to get a good overview about the interaction of all effects and to separate systemetical and stochastic deviations of the measured geometry.

5.1 Theoretical Influence of Simplified Refractive Index Fields on Multiple View Geometry

To analyse the effect of an inhomogeneous refractive index field on the multiple view geometry, we first simplify the set-up to one camera, viewing a single object through two layers with different refractive indices $n_1 > n_2$ (see fig. 10). This reflects the enviroment from Beermann et al. [4] and from section 2.2 adequatly simple, while keeping the characteristics of the different refractive index layers.
The lines of sight from the camera affected by n_2 are refracted towards the more dense medium, i.e. in $y+$-direction. Therefore, an object of known size appears to be smaller than it's size on the camera sensor. When transfering this thought onto optical 3d measurement by multiple view reconstruction, the characteristics of the measured object (e.g. radius, length) should also appear smaller.
The effect of an inhomogeneous refractive index field can only be approximated by this analytical solution, but it provides a good qualitative prediction of what to expect from the measurements. The factor of virtual magnification of an example object can be approximated by the displacement on the camera sensor Δv through *Snellius' law* and trigonometry:

$$\Delta v \propto \arcsin\left(n_1/n_2\right). \tag{3}$$

It is diffucult to acquire an analytical solution for Δv, since the backprojection of the lines of sight through the different layers of refractive indices needs to be calculated. There is a numerical solution, that can be implemented using ray-tracing software, but it is not subject of this paper.

5.2 Influences on Measurement

There are various additional influences on the measurement. The most prominent are due to different effects on the window to the vacuum chamber:

1. different refractive indices of traversed medium on both sides of the window,
2. bending of the window,
3. possible multi-reflections at both surfaces of the window.

Characterisation of these effects can easily be done by measureing the same cold object at ambient and at vacuum pressure. A deviation analysis for this validation has been done and it shows a difference (averaged over three measurements) of less than 2 µm. The radius at 0 atm is slighly smaller than at 1 atm, which was already predicted in section 5.1.
Another influence is the reduced cooling effect of the ambient air at vacuum pressure. Since there was no temperature measurement implemented, there is a chance for some uncertainty. However, for a cylindric heating element made of aluminium oxide Al_2O_3 with a thermal expansion coefficient α of $8.1 \times 10^{-6}\,\mathrm{K}^{-1}$ and an initial radius r_0 of 5.3 mm, for a radius change of 1 µm the element needs to be 23.3 K hotter than before. While the radius difference was shown to be about 10 µm and when abducting 2 µm for the influence of the vacuum, there are still about 8 µm in radius difference left. Those cannot be soley based on the different temperature, since that would mean a temperature difference ΔT of about 200 K.
The calculated radii themselfs are subject to a significant variance (to to 100 µm), depending on their location on the measured cylinder. This, however, does not impact the difference within the calculated radii on one location in different situation. It seems to be more of an issue with the cylindricity of the measured objects and not with the impact of the refractive index field.
The overall influence of the refractive index field seems to be more dependent on the distance in which a refractive index gradient is present than on the absolute refractive index difference. This can easily be detected in figure 8, in which the difference from (90°, 1 atm) to (90°, 0 atm) is significantly smaller than from (180°, 1 atm) to (180°, 0 atm). Also, the (180°, 0 atm) measurements never reach the the calculated radius, i.e. the amount of smaller influence, than the (90°, 0 atm) measurements.

6 CONCLUSIONS

The theoretical assumptions made earlier in this paper fit the re-evaluated and newly acquired results well. Nearly all measurements show a larger radius of the measured object when the measurement is affected by a presumably lesser imhomogeneous refractive index field. The simulations of Beermann [6] also show a similar magnitude of difference between measurements at 1 atm and 0 atm of about 10 µm when comparing them to the measurements in section 4. It also seems to be fair to state that the measured radius

difference apperas to be like sign for both the stated theoretical assumptions of section 5.1 and the measurements.
The magnitude of the deflection effect $|a|$ seems to be proportional to the difference of the optical path $n \cdot d$ length between the assumed geometrical path and the actual path taken by the light:

$$|a| \propto \Delta n \cdot d. \tag{4}$$

7 FUTURE WORK

The ground truth for the measurement of complex geometry of hot objects needs to be established. A possible way to find such a validation database was shown in this paper, even though the already small influence cannot be fully eliminated. A second approach used the incorporation of 2d refractive index measurement or simulation into a virtual fringe projection set-up. The simulated measurement data would be stained by the inhomogeneous refractive index field while the ground truth of the virtual measured data is known. Here are still a couple of issues to solve, e.g. the exact function of the refractive index for temperatures over 100 °C and the instationary nature of the refractive index field. Additionaly, a sufficient fast and easy-to-handle routine for the calibration of a fringe projection system under the influence of vacuum needs to be developed and verified.

ACKNOWLEDGMENTS

The results presented in this paper were obtained within the Collaborative Research Centre 1153 *Process chain to produce hybrid high performance components by Tailored Forming* in the subproject C5 *Multiscale Geometry Inspection of Joining Zones*. The authors would like to thank the German Research Foundation (DFG) for the financial and organisational support of this project.

REFERENCES

[1] H. Eckelmann, *Einführung in die Strömungsmesstechnik*. Teubner Verlag, 1997.

[2] G. Meier, "Hintergrund-Schlierenmeßverfahren. Deutsche Patentanmeldung DE 19942856A1," 21 June 2001.

[3] L. Venkatakrishnan and G. Meier, "Density measurements using the background oriented schlieren technique," *Experiments in Fluids*, vol. 37, pp. 237–247, 2004.

[4] R. Beermann, L. Quentin, A. Pösch, E. Reithmeier, and M. Kästner, "Background oriented schlieren measurement of the refractive index field of air induced by a hot, cylindrical measurement object," *Appl. Opt.*, vol. 56, pp. 4168–4179, May 2017.

[5] ComsolAB, "Comsol Multiphysics." `https://www.comsol.com`, 2017.

[6] R. Beermann, L. Quentin, M. Kästner, A. Pösch, and E. Reithmeier, "Simulation of light deflection due to an inhomogeneous refractive index field induced by a hot measurement object," Proc. DGaO, 2017. To be published.

[7] P. E. Ciddor, "Refractive index of air: new equations for the visible and near infrared," *Appl. Opt.*, vol. 35, pp. 1566–1573, Mar 1996.

[8] The National Institute of Standards and Technology (NIST), "Refractive Index of Air Calculator." `http://emtoolbox.nist.gov/Wavelength/Documentation.asp`, 2017.

[9] D. Stöbener, M. Dijkman, D. Kruse, H. Surm, O. Keßler, P. Mayr, and G. Goch, "Distance measurements with laser-triangulation in hot environments," *integration*, vol. 3, no. 2, p. 5, 2003.

[10] GOM, "GOM Inspect Software." http://www.gom.com/de/3d-software/gom-inspect.html, 2017.

[11] L. Quentin, R. Beermann, A. Pösch, E. Reithmeier, and M. Kästner, "3d geometry measurement of hot cylindric specimen using structured light," in *SPIE Optical Metrology*, pp. 103290U–103290U, International Society for Optics and Photonics, 2017.

[12] L. Quentin, R. Beermann, A. Pösch, M. Kästner, and E. Reithmeier, "3d geometry measurement of hot specimens in different ambient pressure situations," Proc. DGaO, 2017. To be published.

CONTACTS

Dipl.-Ing. Lorenz Quentin lorenz.quentin@imr.uni-hannover.de
Dipl.-Ing. Rüdiger Beermann ruediger.beermann@imr.uni-hannover.de